Chemical Science

Accepted Manuscript

This article can be cited before page numbers have been issued, to do this please use: M. Zhou, M. Zhang, Q. Zhang, X. Ma, H. Fang, H. Dong, X. Chen, J. Sun, L. Li and X. Zhou, *Chem. Sci.*, 2026, DOI: 10.1039/D6SC02904C.

ROYAL SOCIETY OF CHEMISTRY

rsc.li/chemical-science

Minireview

View Article Online

Recent Progress on Iron-Based Hexacyanoferrate for Advanced Potassium-Ion Batteries

Received 00th January 20xx,
Accepted 00th January 20xx

DOI: 10.1039/x0xx00000x

Meng Zhou[a], Mengna Zhang[a], Qian Zhang[a], Xinming Ma[a], Hui Fang[b], Huanhuan Dong[c], Xiang Chen[d,*], Jianchao Sun[e,*], Lin Li[c,*], Xunzhu Zhou[f,*]

Potassium-ion batteries (PIBs) are regarded as promising candidates for large-scale grid energy storage owing to the abundant reserves of potassium resources. Iron hexacyanoferrate (FeHCF), a type of Prussian blue analogue, has garnered significant attention as a cathode material for PIBs due to its robust open framework, high theoretical capacity, and cost-effectiveness. However, the practical application of FeHCF is hindered by its intrinsic limitations, including low electronic conductivity, the presence of interstitial water, and lattice vacancies, which collectively result in inadequate reversible capacity, poor cycling stability and unsatisfactory rate performance. In this review, we summarize the recent achievements of FeHCF cathode materials for PIBs, as well as the key challenges hindering their practical application. In addition, we discuss various modification strategies aimed at enhancing the potassium storage performance, categorizing them into direct approaches (e.g., structural modulation and transition metal doping) and indirect methods (e.g., morphology control, compositing with conductive materials and electrolyte modification). Finally, prospective research directions for improving the electrochemical performance of FeHCF are proposed. This review aims to offer insightful guidance for the rational design of advanced FeHCF materials for high-performance PIBs.

1. Introduction

As the adverse effects of climate change grow increasingly evident, it has become imperative for humanity to shift from traditional fossil fuels (e.g., coal, petroleum, and natural gas) to clean and renewable energy sources such as hydropower, solar, wind, geothermal, and biomass (Fig. 1a).[1-3] However, these renewable energy sources still suffer from significant drawbacks, including intermittency and instability, as they remain highly susceptible to weather conditions, seasonal variations, geographical locations and other influencing factors. These constraints have also given rise to the development of large-scale energy storage technologies (pumped hydro storage, electrochemical energy storage, compressed air energy storage, etc),[4] which enable the continuous and stable output of electricity generated from renewable energy sources. Among the discovered energy storage technologies, electrochemical energy storage technology stands out as a particularly promising candidate due to its advantages such as low maintenance costs and environmental friendliness.

Lithium-ion batteries (LIBs), as a well-established electrochemical energy storage technology, are widely used in daily life. However, their application in large-scale energy storage systems is limited by the scarcity of lithium resources.[5,6] These drawbacks promote the research and development of other alternative metal ion batteries in large-scale energy storage systems, such as sodium-ion batteries (SIBs),[7-11] zinc-metal batteries,[12-15] magnesium-ion batteries[16-18] and potassium-ion batteries (PIBs).[19-23] Among them, potassium-ion batteries (Fig. 1b) are regarded as promising candidates for large-scale energy storage applications based on the following several unique advantages: i) The K/K^+ redox couple exhibits a low standard potential of -2.94 V versus the standard hydrogen electrode (SHE), which facilitates the construction of high-voltage and high-energy-density batteries.[24-26] ii) Potassium is far more abundant in the Earth's crust than lithium (1.5 wt% for K vs. 0.0017 wt% for Li), ensuring greater resource sustainability.[27-29] iii) K^+ possesses a smaller Stokes radius (3.6 Å in PC) compared to Li^+ (4.8 Å) and Na^+ (4.6 Å), attribute to its weaker Lewis acidity, which favors faster ion transport.(Fig. 1c).[30-33] iv) Potassium do not alloy with aluminium at low voltage, therefore the cheaper aluminum foil can be used as the current collector of cathode to replace copper, which can significantly reduce cost in manufacturing PIBs.[34-35]

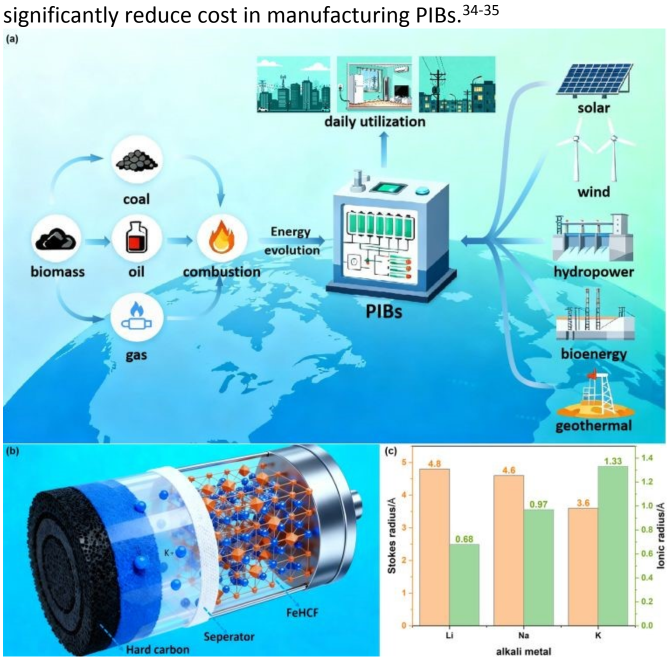

Fig. 1. a) Schematic diagram of the role of large-scale energy storage technology for PIBs in energy structure evolution and energy conversion/storage/utilization. b) Schematic illustration of PIBs using aluminum foil as the current collector. c) Comparison of Stokes radius and ionic radius of Li^+, Na^+, and K^+ in propylene carbonate.

As the core component of PIBs, electrode materials critically determine key performance metrics such as energy density, cycle life, and rate capability. On the anode side, hard carbon and modified graphite has been proved a suitable anode material for PIBs.[36-37] For

a. College of Chemical Engineering and Technology, Yantai Nanshan University, Yantai, Shandong 265713, China.
b. Longkou Donghai Alumina Co.,Ltd. Yantai, Shandong 265713, China.
c. College of Chemistry and Materials Engineering, Wenzhou University, Wenzhou, Zhejiang 325035, China. E-mail: linli@wzu.edu.cn.
d. College of Textile Science and Engineering (International Institute of Silk), Zhejiang Sci-Tech University, Hangzhou 310018, PR China. E-mail: cx9528@zstu.edu.cn
e. School of Environment and Material Engineering, Yantai University, Yantai 264005, China. E-mail: jianchao@ytu.edu.cn
f. Institute School of Materials Science and Engineering, Key Laboratory of Structure and Functional Regulation of Hybrid Material (Ministry of Education), Anhui University, Hefei, Anhui 230601, China. E-mail: xunzhuzhou@ahu.edu.cn

cathodes, various materials have been explored, including layered metal oxides[38-40], polyanionic compounds[41-43], Prussian blue analogs (PBAs)[44-47] and organic cathode materials[48-50]. Among these candidates, layered metal oxides deliver high theoretical specific capacities but generally suffer from structural collapse and rapid capacity fading during repeated K^+ insertion/extraction. Although polyanionic materials exhibit outstanding structural stability, their relatively low specific capacity remains unsatisfactory. Organic cathode materials, despite their structural diversity and sustainability, often suffer from high solubility in electrolytes and poor cycling stability. In contrast, PBAs are regarded as competitive cathode for PIBs for the following aspects: Firstly, their open framework contains large-sized channels that enable rapid K^+ intercalation/deintercalation, leading to superior kinetics. Secondly, high capacity and moderate operating voltage can be achieved by modulating the redox couples of transition metals. Moreover, PBAs can be synthesized through simple methods (e.g., coprecipitation, hydrothermal synthesis), making them cost-effective and suitable for large-scale production.

The general chemical formula of PBAs is represented as $K_xM[M'(CN)_6]_{1-y}\square_y{\cdot}nH_2O$ ($0 \le x \le 2$, $0 \le y \le 1$), where M and M' are transition metal ions (e.g., Fe, Mn, Ni, Co, Cu) and □ stands for the $M'(CN)_6$ vacancy.[51-54] Among them, iron hexacyanoferrate (FeHCF, M and M' = Fe) has garnered significant attention as a cathode material for PIBs. This attention stems from several notable advantages of iron: i) its high crustal abundance and low cost compared to elements like Co and Ni enhance its commercial viability for large-scale applications. ii) the Fe^{2+}/Fe^{3+} redox couple demonstrates high reversibility, contributing to superior cycling stability relative to certain non-iron-based PBAs. iii) the non-toxic and environmentally benign characteristics of iron align well with sustainable development goals. Despite these strengths, existing review articles primarily offer broad overviews of various cathode materials for PIBs. To the best of our knowledge, a systematic review that comprehensively summarizes the research progress on FeHCF for PIBs is still absent.

This review systematically examines the recent advancements in FeHCF cathode materials for high-performance PIBs. It commences with a critical analysis of the fundamental challenges constraining the electrochemical performance and practical application of FeHCF. Subsequently, an in-depth discussion is presented on the effective modification strategies employed to enhance its potassium storage capabilities. The review concludes by proposing insightful perspectives and future research directions for the development of advanced FeHCF-based cathodes.

2. Challenges of FeHCF for PIBs

Although remarkable advancements in FeHCF cathode have been achieved in recent years, significant challenges persist that limit its practical implementation in PIBs. These limitations primarily manifest in three aspects: Firstly, the presence of interstitial water and structural vacancies from conventional synthesis methods, which adversely affect electrochemical reversibility.[55] Secondly, Inadequate structural stability of the framework, which leads to particle pulverization and rapid capacity fade under repeated potassium ion insertion/extraction.[56] Finally, undesirable interfacial side reactions and electrolyte decomposition at high voltages, further compromising the overall storage performances.[57] These interconnected challenges form a multifaceted optimization problem that demands comprehensive material engineering strategies to address synergistically.

3. Modification strategies to boost potassium storage performance of FeHCF

To address the critical challenges currently hindering the practical implementation of FeHCF in PIBs, researchers have developed various modification strategies.[58-62] These optimization approaches can be broadly categorized into two primary groups (Fig. 2): i) Direct modification strategies encompassing crystal structure engineering and elemental doping; ii) Indirect modification strategies involving morphology control, hybridization with conductive material, and electrolyte modification. In this section, we devote to provide a comprehensive review of recent advancements in modification strategies for FeHCF materials in PIBs.

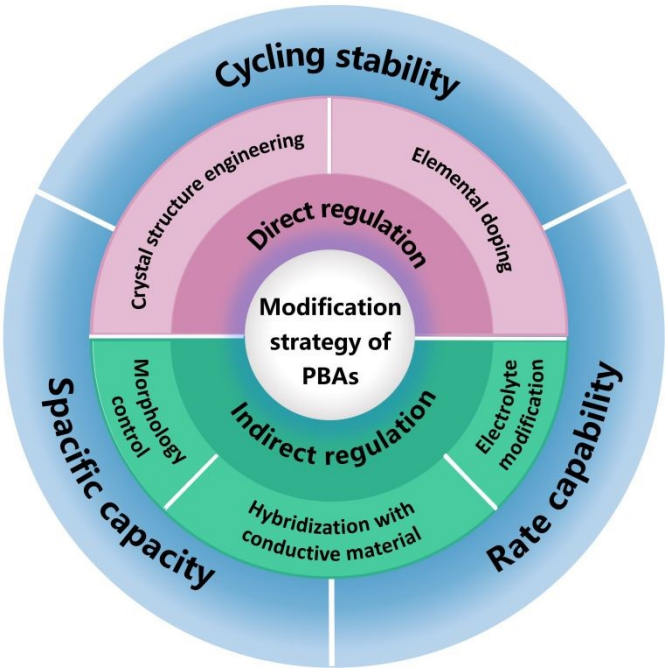

Fig. 2. The modification strategy to boost potassium storage performances of FeHCF.

3.1 Direct modification strategies

3.1.1 Crystal structure engineering

In general, the crystal structure of the FeHCF cathode plays an important role in potassium storage performances. For instance, Li et al. synthesized a series of FeHCF to investigate the effect of crystal structure on the potassium storage performances (Fig. 3a), including irregular Prussian White (PW, $K_{1.64}Fe[Fe(CN)_6]_{0.89}{\cdot}0.895H_2O$), a spindle-like PB ($K_{0.993}Fe[Fe(CN)_6]_{0.997}{\cdot}0.67H_2O$), and a spindle-like PW ($K_{1.72}Fe[Fe(CN)_6]_{0.96}{\cdot}0.342H_2O$).[63] The K-rich spindle-like PW exhibited an obviously improved electrochemical performance, with an initial discharge capacity of 124.2 mAh g^{-1} at the current density of 20 mA g^{-1} as well as a satisfying rate performance (Fig. 3b, c). In situ XRD manifested that the spindle-like PW undergoes no obvious structural evolution and maintains its monoclinic phase during the charge/discharge process (Fig. 3d, e). In addition, density functional theory (DFT) calculations illustrated that the defective PW provides higher energy barriers than the low-defect PW, implying the fast electrochemical reaction kinetics of the spindle-like PW (Fig. 3f, g). They proposed that the high K^+ content, low vacancy, and water content of the spindle-like PW cathode are responsible for the elevated electrochemical performances. To demonstrate the potential of the spindle-like PW for practical application, a spindle-like PW||graphite full cell was assembled (Figure. 3h). As shown in Fig. 3i, j, the spindle-like PW||graphite full cells delivered superior cycling stability (a high capacity retention of 97.4% after 100 cycles) and a high discharge capacity (122.5 mAh g^{-1}). Similarly, Kang's group

prepared two kinds of Prussian Blue cathodes with different content of vacancies and lattice water under the temperatures of 0 °C ($K_{1.36}Fe[Fe(CN)_6]_{0.74}\cdot 0.48H_2O$, PB0) and 25 °C ($K_{1.43}Fe[Fe(CN)_6]_{0.94}\cdot 0.42H_2O$, PB25).[64] The low-defective PB25 exhibited a lower polarization than PB0 during the charge/discharge process. In addition, the elimination of interstitial water provided more space to facilitate K^+ migration and storage, resulting in a significant improvement in the electrochemical performance. As a result, PB25 gave an excellent cycling performance in both half cell and full cell.

Using an electrostatic spray-assisted coprecipitation strategy, Zi and colleagues prepared a $K_2Fe[Fe(CN)_6]$ material, with the chemical formula of $K_{1.56}Fe[Fe(CN)_6]_{0.89}\cdot \square_{0.11}\cdot 1.86H_2O$ (denoted as PBFe@ES).[65] This synthesis method was carried out under an inert atmosphere to effectively inhibit the oxidation of Fe^{2+} into Fe^{3+} and get a highly crystalline sample. Therefore, the PBFe@ES exhibited higher potassium content, fewer vacancies and a larger specific surface area. As a result, the electrochemical performances of PBFe@ES were significantly improved, with an elevated initial discharge specific capacities, better cycling stability and rate performance. Subsequently, Wang et al. employed ethylene diaminetetraacetic acid dipotassium (EDTA-2K) as a strong chelating agent to remove the Fe atoms from the crystal lattice of PBAs during the synthesis process, constructing the Fe^{III} vacancies in Fe-based PBAs.[66] They found that the existence of Fe^{III} vacancies can effectively restrain the lattice distortion and prevent the structural deformation. Therefore, the PBAs with Fe^{III} vacancies show an improvement in the electrochemical stability. To obtain a FeHCF with a superior crystal structure, Ma et al. proposed a dual-salt (potassium citrate (K-CA) and potassium chloride (KCl)) assisted co-precipitation method for fabricating cubic-like monoclinic high-quality $K_{1.64}FeFe(CN)_6$ (denoted as PW-HQ) with less crystalline water (6.21%).[67] The chelator K-CA could slow down the nucleation process and the following crystal growth by chelating coordination with iron ions, while the KCl can increase the K^+ content, adjust the morphology and eliminate the interstitial water of the material. Noticeably, K ions were not completely extracted from the monoclinic structure and the remaining K ions were estimated to support the crystal structure during the charge/discharge process, ensuring a superior structural stability. Therefore, the PW-HQ delivers a high capacity retention of 93% after 1000 cycles at 200 mA g^{-1}. Shu et al. also realized a better control of the crystallization process to prepare $K_{1.61}Fe[Fe(CN)_6]_{0.88}\cdot 0.43H_2O$ (denoted as KFeHCF-E) with high crystallinity by using EDTA-2K as the chelating agent.[68] Compared with the material synthesized without the addition of EDTA-2K, the KFeHCF-E exhibited an elevated specific capacity, a high rate performance and an outstanding cycling stability. Recently, Zhang and colleagues developed a novel reaction environment-tailored strategy for the synthesis of high-quality PB.[69] During the synthesis process, a mother liquor, containing a concentrated potassium bis(fluorosulfonyl)imide (KFSI)/water was employed to provide a high K^+ concentration and low activity of free water. Thus, the prepared PB material $K_{1.69}Fe[Fe(CN)_6]_{0.95}\square_{0.05}\cdot 0.74H_2O$ (PB-ML) exhibited a highly crystallinity with a remarkably low $[Fe(CN)_6]^{4-}$ vacancies (denoted as V_{FeCN}) content (5%) and a minimized crystal water content (3.98%), while the V_{FeCN} content and crystal water content of $K_{1.08}Fe[Fe(CN)_6]_{0.74}\square_{0.26}\cdot 1.24H_2O$ (PB-W) prepared via a water-based coprecipitation method is much higher. Especially, the cycling performance of PB-ML was greatly improved which presented an outstanding cyclic stability with a capacity retention of 71.3% after 2500 cycles at 50 mA g^{-1} and 67.5% after more than 20,000 cycles at 500 mA g^{-1}, much better than that of PB-W.

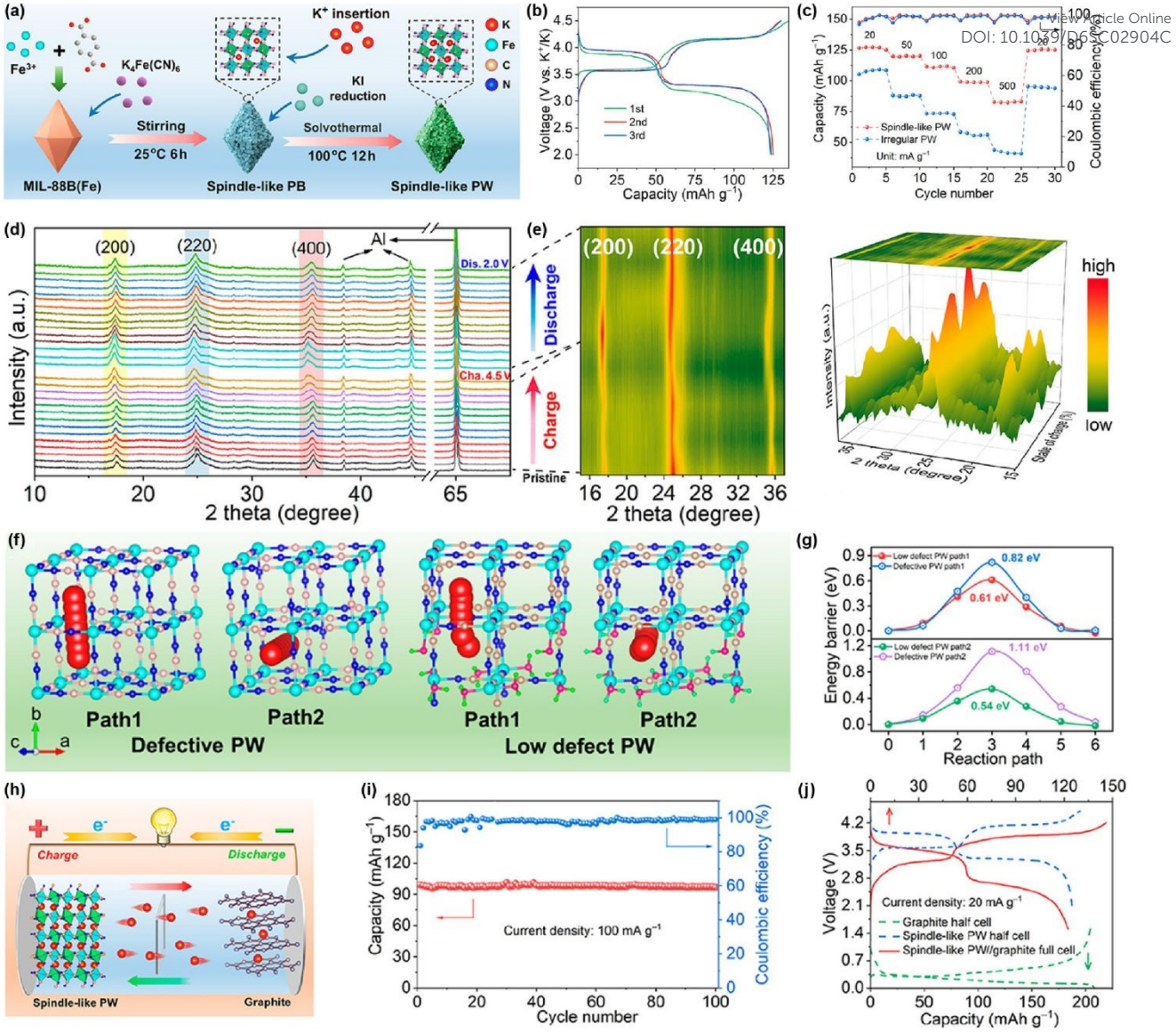

Fig. 3. a) Schematic description of the formation procedure of spindle-like PW. b) The charge/discharge profiles of the spindle-like PW cathode. c) Rate performances of spindle-like PW and irregular PW. d) In situ XRD patterns and e) the relevant 2D and 3D contour maps of spindle-like PW. f) Schematic illustration of possible K^+ migration paths for the defective and low-defect PWs. g) Corresponding migration energies of the two paths in the defective and low-defect PWs. h) Schematic plots of spindle-like PW||graphite full cell and i) Cycling performance of the spindle-like PW||graphite full cell at 100 mA g^{-1}. j) Typical charge/discharge curves of the spindle-like PW||graphite full cell. Reproduced with permission.[63] Copyright 2023, American Chemical Society.

3.1.2 Transition metal element doping

Element doping can effectively enhance the structural stability of FeHCF, significantly improve its potassium storage performance.[70-72] Huang et al. proposed that doping with appropriate amount of Ni may activate the C-coordinated $Fe^{2+}C_6/Fe^{3+}C_6$ redox couple, inducing an increase in high-voltage plateau capacity.[73] Among the prepared samples, $K_{1.63}Ni_{0.05}Fe_{0.95}[Fe(CN)_6]_{0.92}\cdot 0.42H_2O$ showed the best electrochemical performance, with an initial discharge capacity of 135 mAh g^{-1}. Subsequently, Qiao et al. utilized a medium entropy concept to synthesize a potassium manganese iron copper hexacyanoferrate ($K_{1.90}Fe_{0.67}Mn_{0.16}Cu_{0.09}\square_{0.09}[Fe(CN)_6]\cdot 1.78H_2O$).[35] The incorporation of the inert Cu-ion with large electronegativity endowed a robust Cu-N bond and a superior structural stability of the material, enabling the cathode material to undergo a zero-stress solid-solution reaction during the charge/discharge process. Therefore, the as-prepared material delivered a high initial discharge capacity of 127.5 mAh g^{-1}, a significantly enhanced rate performance and an excellent cycling stability with a high-capacity retention of 90.7% after 100 cycles. Recently, Zhou's group reported a Mn-substituted KFHCF ($K_{1.81}Fe_{0.90}Mn_{0.10}[Fe(CN)_6]_{0.95}\cdot 0.92H_2O$, KMFHCF-0.1) for PIBs.[74] As shown in Fig. 4a-c, a small amount of high-spin Mn (MnHS-N) substitution can effectively reduce the band gap and energy barrier for K^+ migration. Meanwhile, the low-spin Fe coordinated with carbon atoms (FeLS-C) is activated after Mn substitution, resulting in an increased reversible capacity (Fig. 4d, e). Compared with unsubstituted KFHCF ($K_{1.78}Fe[Fe(CN)_6]_{0.94}\cdot 1.01H_2O$), KMFHCF-0.1 exhibited a high discharge capacity of 135 mAh g^{-1}, with a capacity retention of 85% after 50 cycles (Fig. 4f, g). More importantly, the KMFHCF-0.1||hard carbon full cell demonstrated an excellent rate performance(Fig. 4h), a high reversible capacity of 110 mAh g^{-1} and a considerable energy density of 275 Wh kg^{-1} (Fig. 4i).

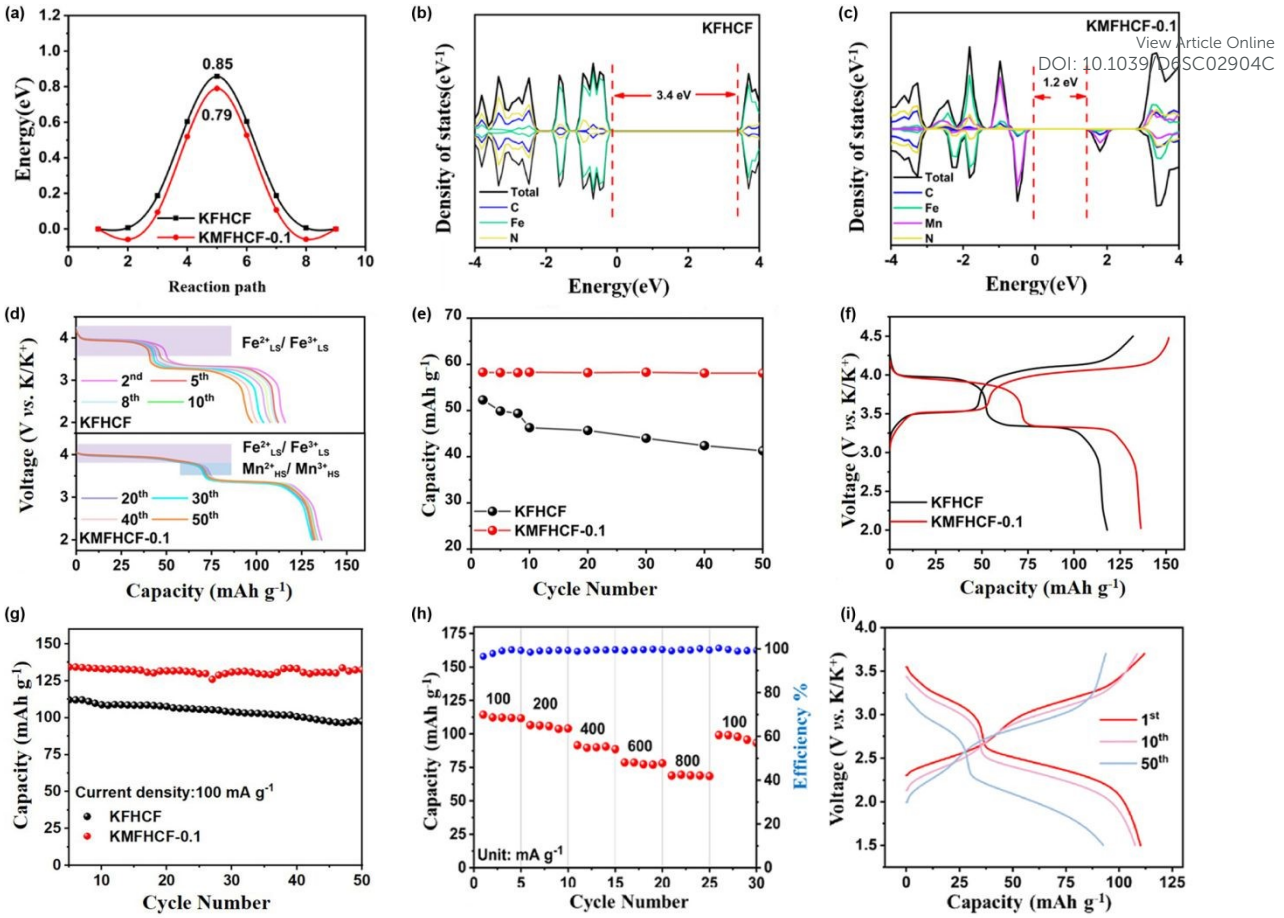

Fig. 4. a) The energy barriers of K^+ diffusion in KFHCF and KMFHCF-0.1, respectively. The density of (DOS) states for b) the KFHCF and c) KMFHCF-0.1 model structures. The Fermi energy is set as zero. d) Discharge curves at different cycles and e) the corresponding capacity contribution of FeLS-C voltage platform after various cycles at the current density of 100 mA g^{-1}. f) First charge /discharge patterns of KFHCF and KMFHCF-0.1 at 100 mA g^{-1}, respectively. g) Cycling performance of KFHCF and KMFHCF-0.1 at the current density of 100 mA g^{-1}. h) Rate capability of KMFHCF-0.1. i) Cycling performance at 100 mA g^{-1}. Reproduced with permission.[74] Copyright 2023, Elsevier.

Similarly, Zhou et al. constructed a defect-free potassium iron manganese hexacyanoferrate ($K_{1.47}Fe_{0.5}Mn_{0.5}[Fe(CN)_6]\cdot 1.26H_2O$, KFMHCF-1/2) as cathode material for PIBs.[75] Fe and Mn binary synergy can increase the entropy in the cation positions coordinated with N atom, which can effectively suppress $[Fe(CN)6]^{4-}$ anionic defects based on charge balance, thus generating a vacancy-free PBA cathode material and improving the electrochemical performances. Via DFT calculations and dynamics analysis, they evidenced the band gap and K-ion diffusion barrier can be obviously reduced, thus, achieving excellent electronic and K^+ transport kinetics. Importantly, Mn and Fe as dual active centers enabled an ultrahigh specific capacity of 155.3 mAh g^{-1} at 10 mA g^{-1} with the energy density of 599.5 Wh kg^{-1}, superior cyclic stability of over 450 cycles at 50 mA g^{-1}. The full cell using K deposited on graphite (K@G) as anode and KFMHCF-1/2 as cathode also delivered a long lifespan of over 1000 cycles at 50 mA g^{-1} with the lowest capacity decay rate of 0.044% per cycle. In addition, Huang et al. synthesized three different samples with the chemical composition of $K_{1.08}Fe[Fe(CN)_6]_{0.62}\cdot 1.64H_2O$ (KFHCF), $K_{1.68}Mn[Fe(CN)_6]_{0.88}\cdot 1.90H_2O$ (KMHCF) and $K_{1.30}Fe_{0.42}Mn_{0.45}Sn_{0.13}[Fe(CN)_6]_{0.94}\cdot 1.35H_2O$ (KFMSHCF). Among these three samples, entropy engineering and d^{10} cation incorporation constructed KFMSHCF performed best as cathode materials for PIBs.[76] The construction of a high configurational entropy increases cation disorder at N-coordinated sites, therefore, effectively suppressing the $[Fe(CN)_6]^{4-}$ vacancies. And the entropy-induced cation disorder also boosts KFMSHCF to exhibit reduced band gap and low K-ion diffusion barrier (Fig. 5a, b), thereby ensuring excellent electrochemical kinetic (Fig. 5c, d). And the entropy stabilization effect as well as strong Sn−N coordination induced by the completely occupied d^{10} configuration of Sn^{2+} can restrain serious lattice distortion with a structural evolution from monoclinic to cubic which can be verified by in-situ XRD (Fig. 5e, f), enabling reversible K^+ storage, with a high reversible energy density of 364.2 Wh kg^{-1} and long-term cycling stability of more than 300 cycles at 100 mA g^{-1} with the capacity retention of 82.1%. This tailored structure also enabled the full cell an excellent durability over 2500 cycles with an ultralow capacity fading rate of only 0.017% per cycle and a superior initial energy density compared with other reported cathodes (Fig. 5g, h).

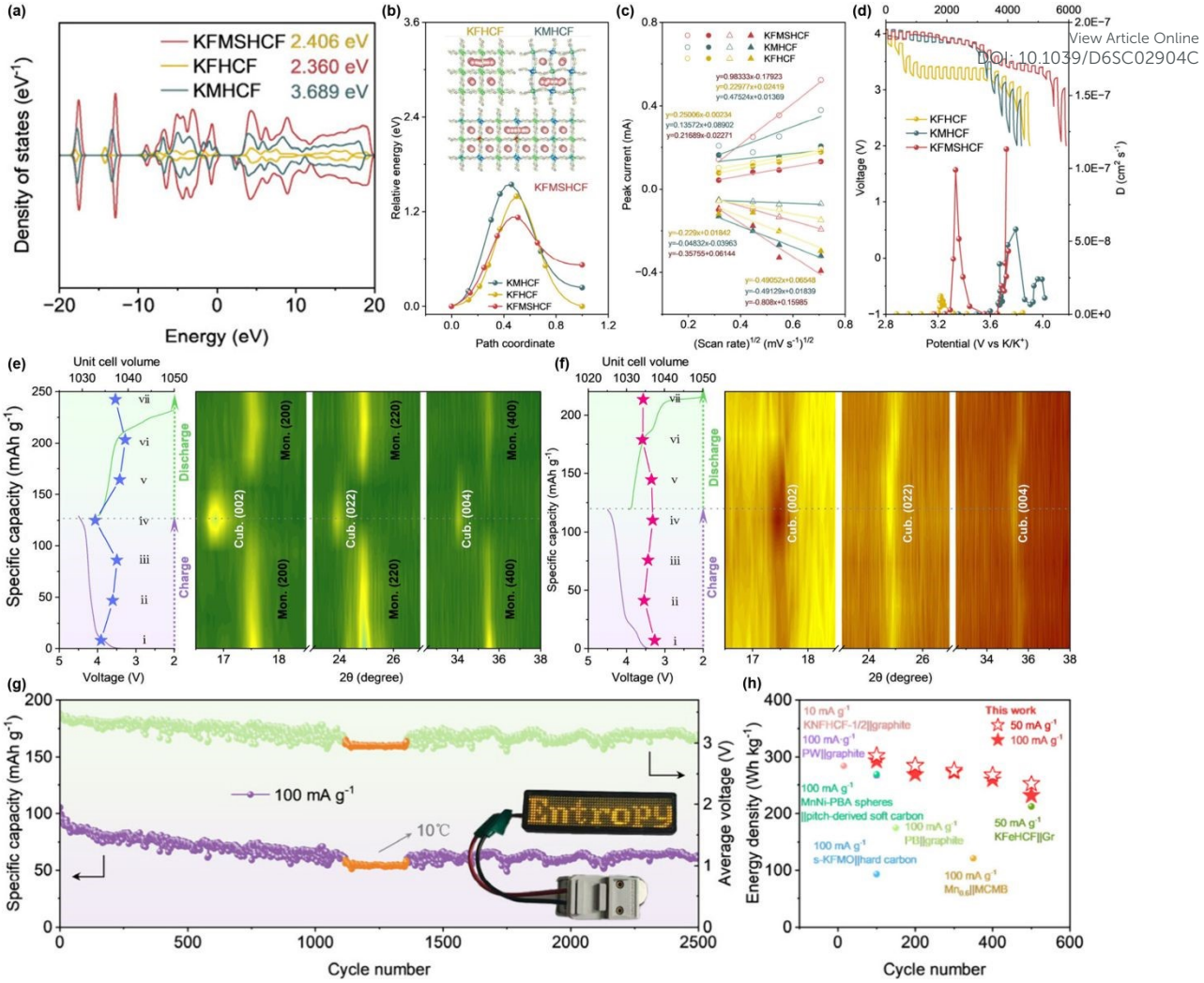

Fig. 5. a) DOS plots and b) Calculated K-ion diffusion barrier of the three electrodes. c) Linear fitting relationship of I_p vs $v^{1/2}$ and d) Galvanostatic Intermittent Titration Technique (GITT) profiles and corresponding K^+ diffusion coefficients. The initial charge/discharge curves and intensity contour maps of XRD for e) KMHCF and f) KFMSHCF. g) The long-term cycling performance of KFMSHCF||graphite full cell at 100 mA g^{-1}. h) Comparison of the cycle life and initial energy density of published work. Reproduced with permission.[76] Copyright 2025, American Chemical Society.

3.2 Indirect regulation

3.2.1 Morphology design

Morphology design can effectively shorten the K^+ diffusion path and facilitate electrolyte permeation, resulting in an improved potassium storage performance of electrode materials. Chong and coworkers reported a $KFe[Fe(CN)_6]_{0.82}\cdot 2.87H_2O$ nanoparticle with 3D open framework for PIBs.[77] Ex-situ XRD confirmed the great structural stability of the material during the charge/discharge process. Therefore, a superior cycling stability (a high capacity retention of 80.49% after 1000 cycles) was achieved. The effect of the crystallite size of Prussian blue-based cathode on electrochemical performance is investigated by Nazar's group.[78] They synthesized three samples with different crystallite size (nano ($K_{1.69}Fe[Fe(CN)_6]_{0.90}\cdot 0.4H_2O$, KFeHCF-S), submicron ($K_{1.78}Fe[Fe(CN)_6]_{0.92}\cdot 0.4H_2O$, KFeHCF-M), and micron ($K_{0.68}Fe[Fe(CN)_6]_{0.89}\cdot 0.7H_2O$, KFeHCF-L) crystallites) by a novel citrate chelation route for the first time. Compared with KFeHCF-M and KFeHCF-L, KFeHCF-S showed a highest reversible capacity of 140 mAh g^{-1}. Noticeably, KFeHCF-S cathode with nano-crystallite particles delivered a comparable energy density (~500 Wh kg^{-1}) to that of sodium HCF cathodes.

Mai's group synthesized an ultrathin nanosheet-assembled flower-like hierarchical Prussian blue materials ($K_{1.4}Fe_4[Fe(CN)_6]_3$, PB-NSs) by a facile dissolution-recrystallization strategy.[79] Benefiting from the hierarchical structure, more active sites were exposed and the diffusion path was greatly shortened, thereby promoting the efficient K^+ diffusion and leading to the enhanced electrochemical performance of PB-NSs. In addition, the XRD results revealed that the lattice structure of PB-NSs during the charge/discharge process was well-maintained, indicating the superior stability of PB-NSs. Subsequently, Xu et al. obtained mesoporous single-crystalline iron hexacyanoferrate ($K_{0.0216}FeFe(CN)_6\cdot 3.03H_2O$, MSC-FeHCF) microspheres by using a SiO2 template-assisted synthesis strategy. (Fig. 6a-c).[80] This unique mesoporous micro-structure not only facilitates the permeation of the electrolyte and fastens the K^+ migration, but also relieves the internal stress of MSC-FeHCF during cycling and restricts the interstitial water content inside the material (Fig. 6d, e). Meanwhile, the single crystal decreases grain boundaries, enabling fast charge transfer (Fig 6f), therefore, the MSC-FeHCF delivers a superior cycling stability and rate performance of 86.7 mAh g^{-1} at 3 A g^{-1} and retain 85.8% of the specific capacity after 2000 cycles at 0.5 A g^{-1}. As shown in Fig 6g, h, in situ XRD revealed a reversible phase transition from the cubic phase to the monoclinic phase during the charge/discharge process.

View Article Online
DOI: 10.1039/D6SC02904C

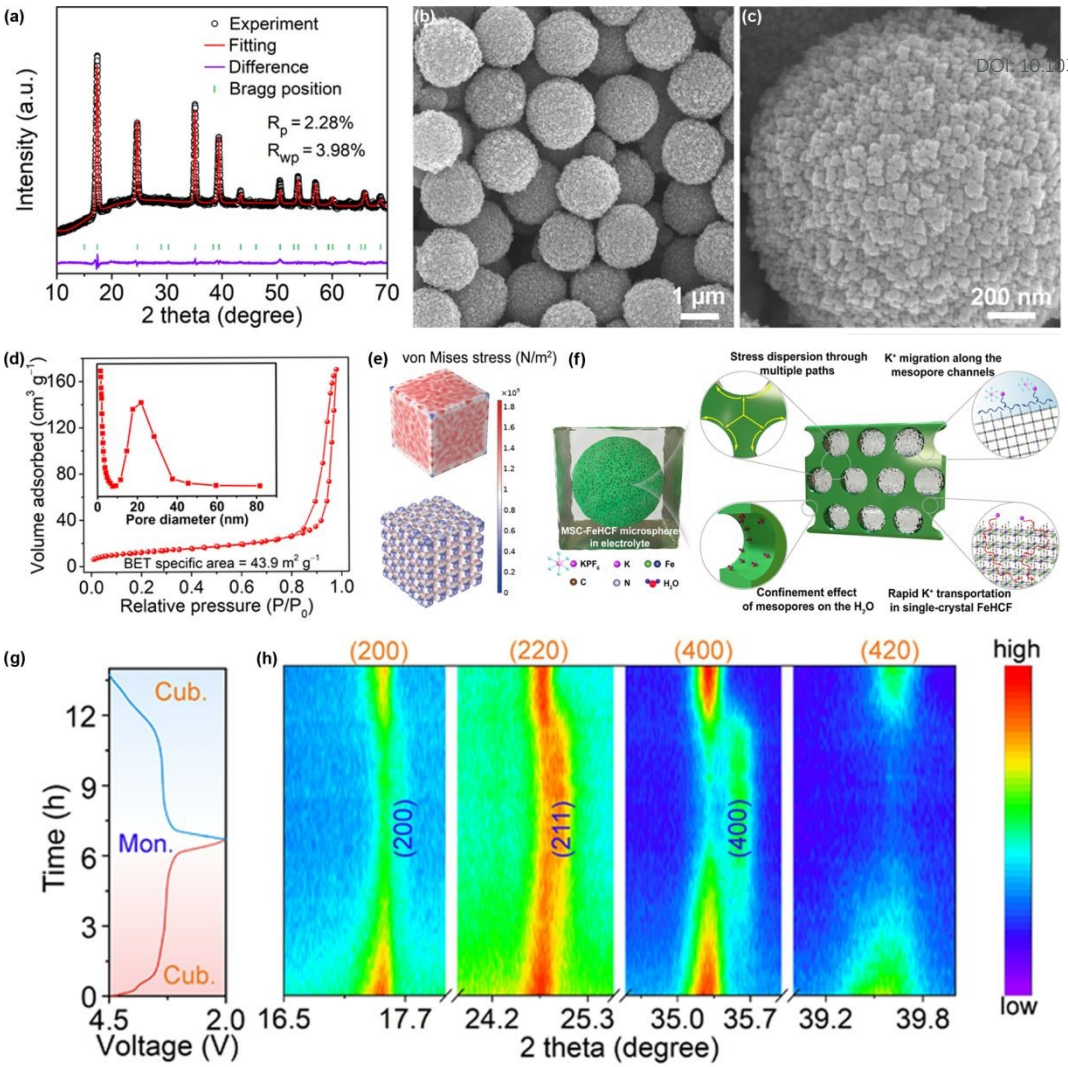

Fig. 6. a) Rietveld refinement on XRD pattern of MSC-FeHCF. b) and c) SEM images of MSC-FeHCF microspheres. d) BET analysis of MSC-FeHCF. Inset: pore size distribution. e) Von Mises stress contours of MSC-FeHCF (top) and MSC-FeHCF (bottom) stress with complete potassiation. f) Schematic illustration of stress dispersion, mesoporous confinement effect, electrolyte full wetting, and rapid K^+ transportation in MSC-FeHCF. g) Charge/discharge curves of MSC-FeHCF. h) The relevant 2D contour plots of in situ XRD patterns. Reproduced with permission.[80] Copyright 2025, Wiley-VCH.

3.2.2 Composite with conductive materials

In general, composites with conductive materials can enhance charge transfer efficiency and alleviate volume changes during charge and discharge processes, thereby effectively improve potassium storage performance. Xue et al. synthesized a polypyrrole-modified Prussian blue material $K_{1.87}Fe[Fe(CN)_6]_{0.97}\cdot\square_{0.03}\cdot 0.84H_2O$ (KHCF@PPy) through an in situ polymerization coating method.[81] The introduction of conductive polypyrrole effectively enhanced the electronic conductivity of KHCF, resulting in improved rate capability of the KHCF@PPy cathode. In addition, ex-situ XRD demonstrated the superior structural stability of KHCF@PPy during the charge/discharge process. Benefiting from the above merits, KHCF@PPy exhibited an initial discharge capacity of 88.9 mAh g^{-1} and superior cycling stability with a capacity retention of 85% after 500 cycles. Similarly, Zhou et al. designed a polypyrrole modified Prussian blue $K_{0.97}Fe[Fe(CN)_6]_{0.83}\cdot\square_{0.17}\cdot 0.28H_2O$ (PB-PPY).[82] They found that part of K^+ remain in the PB-PPY framework and act as the pillars, ensuring fast K^+ diffusion kinetics and strengthening the stability of the PB framework (Fig. 7a). Therefore, the as-prepared PB-PPY displayed a higher discharging capacity of 108.6 mAh g^{-1} for the first cycle than that of pure Prussian blue (55.5 mAh g^{-1}) (Fig. 7b, c). Ex-situ XRD analysis during the first two cycles of charge and discharge evidenced that there is no phase transition for the PB-PPY sample and the storage mechanism can be asigned to a solid solution reaction (Fig. 7d, e). Also, compared with the pure PB, the PB-PPY sample exhibited a better rate capability and an obviously outstanding cycling stability (Fig. 7f, g).

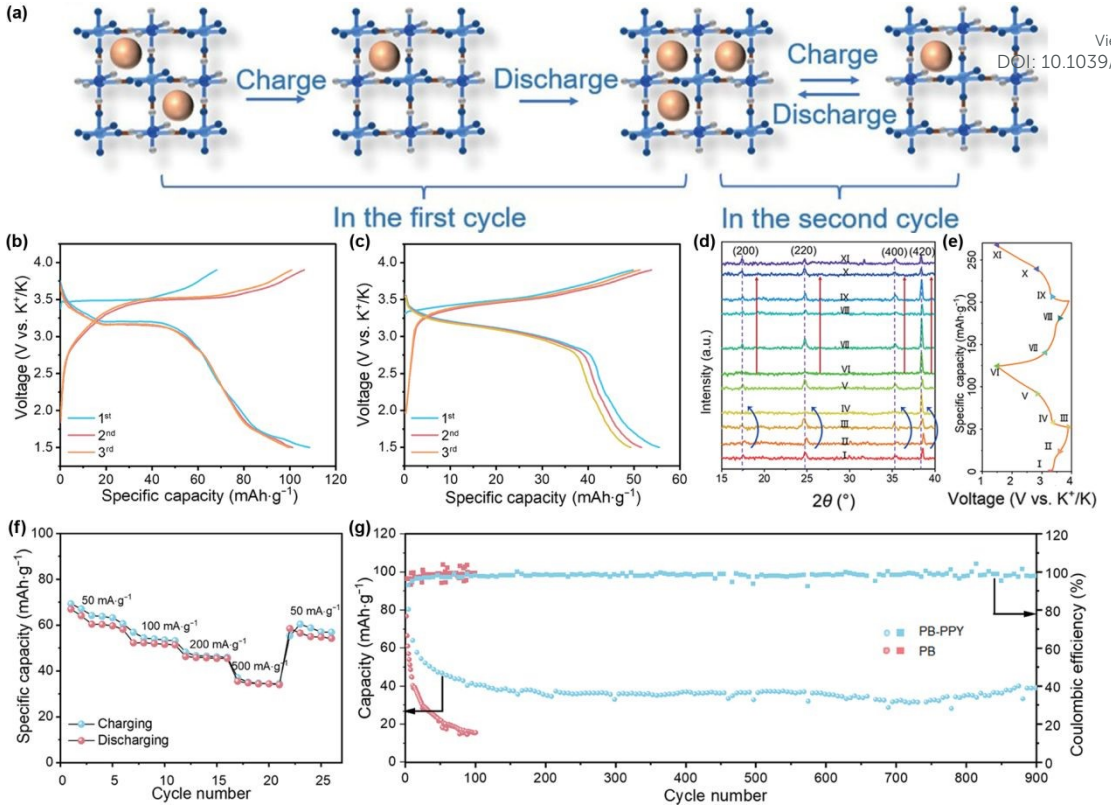

Fig. 7. a) The schematic illustration of K ions storage mechanism of PB. Charge/discharge curves of b) PB-PPY sample and c) PB sample at 50 mA g^{-1}. d) Ex-situ XRD patterns at different charge/discharge states. e) The first two cycles charge/discharge curves of PB-PPY. f) Rate capability of PB-PPY at different current densities of 50-500 mA g^{-1}. g) Cycling comparison of PB and PB-PPY at a current density of 50 mA g^{-1}. Reproduced with permission.[82] Copyright 2023, Springer.

In addition, Zhu et al. created a synthesis method via transformation of the corrosion layer of rusty stainless-steel meshes (RSSM) into compact stack-layers of Prussian blue (PB) nanocubes, when furthercoated with reduced graphite oxide (RGO), they fabricated a flexible binder-free electrode (denoted as RGO@PB@SSM) for PIBs.[83] The unique structure not only enhances the conductivity but also improves the structural stability of the electrode. Therefore, RGO@PB@SSM cathode showed a high initial discharge capacity of 96.8 mAh g^{-1}, rate performance (43 mAh g^{-1} at 400 mA g^{-1}) and cycling stability (capacity retention of 75.1% after 305 cycles). Subsequently, Wei and coworkers investigated a series of PB/GO-based composites, $K_{1.50}Fe[Fe(CN)_6]_{0.90}\cdot 0.34H_2O$/GO (PB/GO), $K_{1.56}Fe[Fe(CN)_6]_{0.91}\cdot 0.33H_2O$/rGO (PB/rGO) and $K_{1.59}Fe[Fe(CN)_6]_{0.90}\cdot 0.30H_2O$/PVP-rGO (PB/PVP-rGO).[84] Noticeably, some oxygen-containing functional groups were lost during GO reduction, thus weakening the PB and rGO interaction, leading to the structural destruction of PB with poor electrochemical performance. They found that the presence of PVP facilitated the repaired interaction between rGO and PB, which ensured the integrity of the carbon-encapsulating structure and the conductivity of the PB/PVP-rGO cathode in the long-term cycling. Among these composited materials, PB/PVP-rGO exhibited the best potassium storage performance, with a high-capacity retention of 96.5% after 800 cycles. Finally, they fabricated a potassium-ion full-cell with pre-potassiation intercalated graphite (KC8) as anode, which exhibited outstanding rate performance (77.0 mAh g^{-1} at 10 C) and excellent cycling ability (a high capacity retention of 88.1% after 150 cycles).

Recently, Liu et al. pointed out that hybrid cathode design may offer promising solutions to capacity improvement by introducing a novel anion-cation relay storage mechanism.[85] Using MoS_2/carbon fibers (CFs) as both a conductive additive and an anion host, they innovatively prepared a prussian blue analogues-based hybrid cathode (PBAs-MoS_2/CFs, Fig. 8a-f). As shown in Fig. 8g-i, the galvanostatic charge/discharge (GCD) profiles of PBAs-MoS_2/CFs hybrid cathode showed combination characteristics of both the MoS_2/CFs cathode and the PBAs cathode GCD profiles, which implied an anion-cation relay process within the hybrid cathode, that is K^+ ions undergo insertion/extraction in the PBAs component, while PF^{6-} ions are inserted into/extracted from the MoS_2/CFs part. This synergistic mechanism of dual-ion within hybrid cathode significantly enhances electrochemical performances in capacity, rate capability and lifespan (Fig. 8j, k). Therefore, the PBAs-MoS_2/CFs hybrid cathode exhibited an ultrahigh specific capacity of ≈143.8 mAh g^{-1} at 100 mA g^{-1} and maintained a capacity retention of over 87.4% after 500 cycles at 1000 mA g^{-1}.

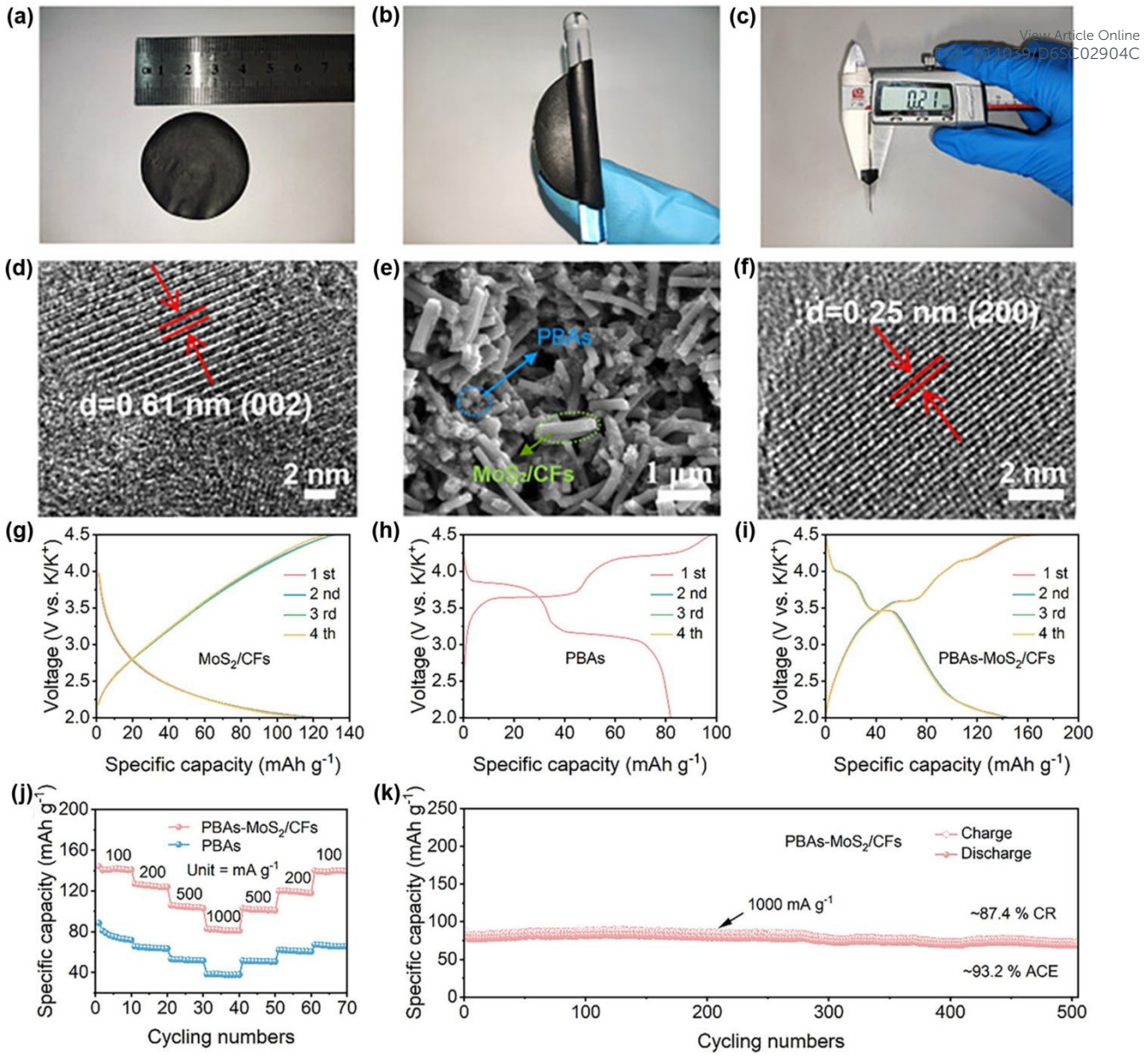

Fig. 8. a-c) Optical images of PBAs-MoS_2/CFs. d, f) High-resolution TEM images of MoS_2 and PBAs, respectively. e) SEM image of PBAs-MoS_2/CFs hybrid electrode. g-i) charge/discharge curves of MoS_2/CFs, PBAs and PBAs-MoS_2/CFs at a current density of 100 mA g^{-1}. j) rate performance of PBAs-MoS_2/CFs under different current densities from 100 to 1000 mA g^{-1}. k) cycling stabilities of PBAs-MoS_2-CFs at a current density of 1000 mA g^{-1}. Reproduced with permission.[85] Copyright 2025, Wiley-VCH.

3.2.3 Electrolyte modification

Electrolytes, often regarded as the "blood" of batteries, critically determine their electrochemical performance. Jeschull and coworkers presented a poly(ethylene oxide)-potassium bis(trifluoromethanesulfonyl)imide (PEO-KFTSI) solid polymer electrolyte (SPEs) for the Prussian blue analogue cathode electrode ($K_2Fe[Fe(CN)_6]$).[86] Compared with traditionally organic liquid electrolytes, the $K_2Fe[Fe(CN)_6$ cathode with SPEs exhibited a significantly improved potassium storage performance. Moreover, Lin et al. proposed a dual stabilization strategy to improve the reversible capacity and electrochemical stability of Potassium Prussian Blue (KPB).[87] They applied ethylenediaminetetraacetic acid dipotassium salt (EDTA-2K) as the chelating agent to adjust the crystallization process during co-precipitation. Meanwhile, potassium bis (fluorosulfonyl) imide (KFSI) was employed to construct a robust cathode/electrolyte interface. As a result, the KPB||graphite full cell exhibited a high reversible capacity of 102.4 mAh g^{-1}, good rate performance (40.4 mAh g^{-1} at 1.5 A g^{-1}) and superior cycling stability (88% capacity retention from cycle 25 to 400). Subsequently, Wang and colleagues developed a dual additive modification strategy to regulate the interface chemistry of Fe-based Prussian blue analogs (KFeHCF) cathode.[88] The theoretical calculations and CV analysis evidenced that potassium selenocyanate (KSeCN) is easier to be oxidized on the cathode surface and facilitates the formation of robust cathode electrolyte interphase (CEI) (Fig. 9a-c) which can remarkably inhibit the side reactions during electrochemical process and therefore gives an improved cycling stability. They proposed that the dual-additive can dramatically alleviate Fe dissolution and stabilize the KFeHCF structure (Fig. 9d-f). The K||KFeHCF cell with optimized electrolyte achieved a superior cycling performance (a high capacity retention of 81.5% after 5000 cycles) compared with the electrolyte without additives (17.7% of its original capacity after 1000 cycles) and other reported works (Fig. 9g, h).

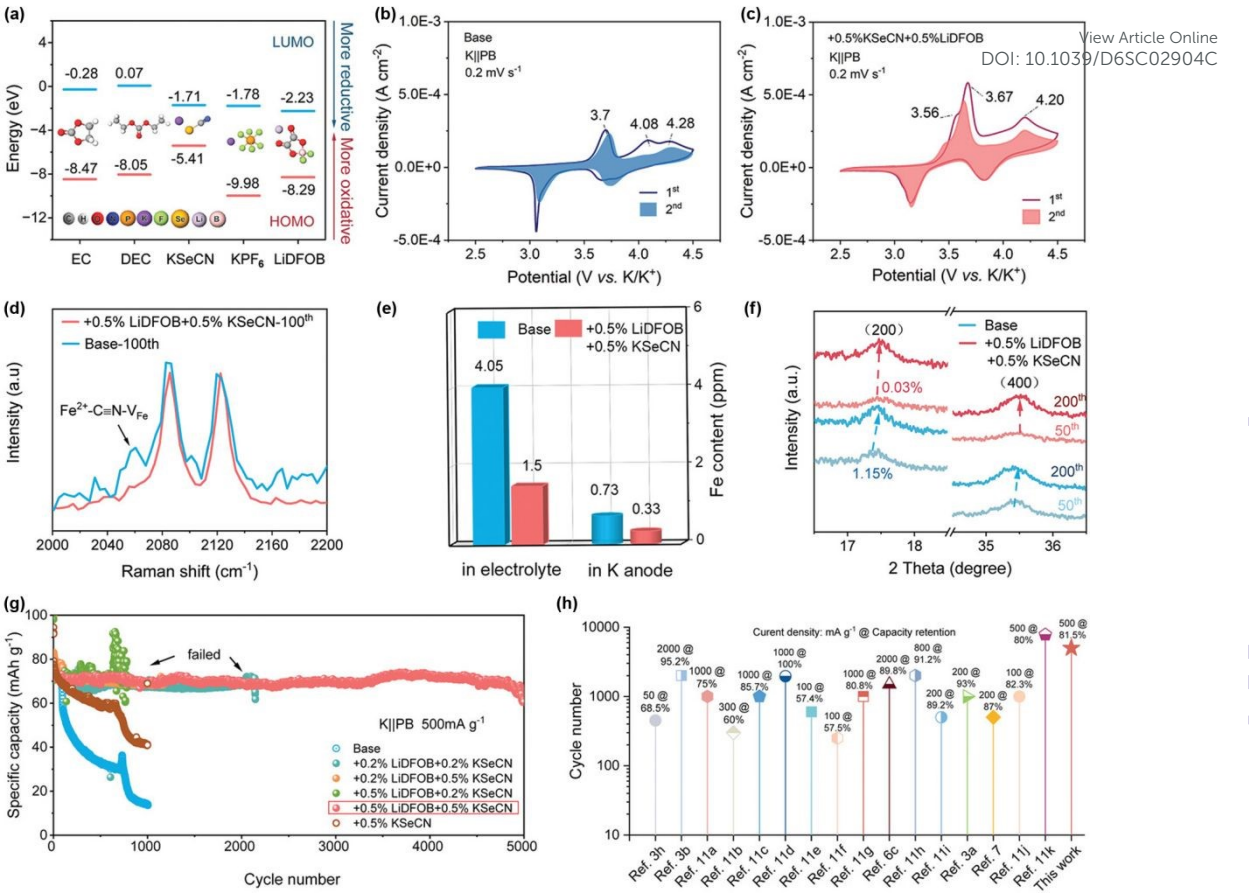

Fig. 9. a) Calculation of HOMO and LUMO of conventional solvent components, KSeCN and LiDFOB. CV tests of the KFeHCF electrode measured at scan rate of 0.2 mV s^{-1} in b) base electrolyte and c) electrolyte with 0.5 wt.% KSeCN + 0.5 wt.% LiDFOB. d) Raman analysis of KFeHCF cathode with base and optimized electrolytes after 100 cycles. e) ICP-OES results of the base and optimized electrolytes after 100 cycles. f) Ex-situ XRD curves of KFeHCF cathode at different cycles with base and optimized electrolytes. g) Cycling performance comparison of base and dual-additive electrolytes under 5C charge and discharge rates. h) Comparison of the cycling life of K||KFeHCF batteries with previously reported works. Reproduced with permission.[88] Copyright 2025, Wiley-VCH.

4. Conclusions and perspectives

Owing to their cost-effectiveness, open framework, and high theoretical capacity, FeHCF have emerged as promising cathode materials for PIBs. This review has comprehensively summarized the recent advancements in FeHCF, highlighting its potential while critically addressing the key challenges that impede practical application (such as low electronic conductivity, the presence of interstitial water, and structural vacancies), all of which lead to inadequate capacity reversibility, limited cycling stability and unsatisfactory rate performance. From a commercial application standpoint, we have discussed a range of strategic modification approaches to effectively mitigate these issues. To enable the practical application of FeHCF cathodes in PIBs, they should meet the following performance milestones in the future: reversible capacity $\geqslant$ 130 mAh g^{-1} and capacity retention $\geqslant$ 80% after 2000 cycles. Furthermore, to facilitate a clear comparison of the development status of various FeHCF-based materials, the electrochemical performance metrics of representative candidates are systematically summarized in Table 1. Generally, crystal structure engineering and elemental doping can effectively enhance the structural stability of the FeHCF cathode, thereby extending its cycle life. In addition, morphology control and hybridization with conductive materials can significantly improve charge transfer kinetics, thus enhancing the rate capability of FeHCF.

Table 1. The electrochemical performance of some representative iron-based hexacyanoferrate for PIBs.

Classification	Materials	Voltage range (V versus K^+/K)	Initial discharge capacity (mAh g^{-1})	Rate performance (mAh g^{-1})/current density (mA g^{-1})	Cycling stability (capacity retention %/cycles)	Initial Coulombic efficiency (%)	Electrolyte	Ref.

View Article Online
DOI: 10.1039/D6SC02904C

Direct regulation	Crystal structure engineering	$K_{1.72}Fe[Fe(CN)_6]_{0.96}\cdot 0.342H_2O$	2.0-4.5	124.2	82.7/500	89.2/500	92.1	5 M KFSI DEGDME	63
		$K_{1.43}Fe[Fe(CN)_6]_{0.94}\cdot 0.42H_2O$	2.5-4.3	109.8	54.1/1000	86.5/1000	-	0.5 M KPF_6 EC/DEC	64
		$K_{1.56}Fe[Fe(CN)_6]_{0.89}\cdot \square_{0.11}\cdot 1.86\ H_2O$	2.0-4.4	118	82/1550	76/503	105.3	0.8 M KPF_6 EC/DEC + 1 wt% FEC	65
		$K_{1.74}FeFe(CN)_6$	2.0-4.0	79.4	45/200	57.5/250	97	0.8 M KPF_6 EC/DEC + 1% FEC	66
		$K_{1.64}FeFe(CN)_6$	2.0-4.3	113.1	60.4/1000	93/1000	-	2.5 M KFSI TEP	67
		$K_{1.61}Fe[Fe(CN)_6]_{0.88}\cdot 0.43H_2O$	2.0-4.0	77.0	60.1/100	61.3/5000	104	2.5 M KFSI TEP	68
		$K_{1.69}Fe[Fe(CN)_6]_{0.95}\square_{0.05}\cdot 0.74H_2O$	2.0-4.3	124.8	73/1000	71.3/2500	-	2.5 M KFSI TEP	69
		$K_{1.68}Fe_{1.09}Fe(CN)_6\cdot 2.1H_2O$	2.0-4.5	110.5	-	81/100	105.1	0.8 M KPF_6 PC +4 wt% FEC	89

	Transition metal element doping	$K_{1.90}Fe_{0.67}Mn_{0.16}Cu_{0.09}□_{0.09}[Fe(CN)_6]·1.78H_2O$	2.0-4.5	127.5	63.7/200	~70/350	-	1 M KPF_6 EC/DEC/PC	36
		$K_{1.63}Ni_{0.05}Fe_{0.95}[Fe(CN)_6]_{0.92}·0.42H_2O$	2.0-4.5	~135	81/400	94.4/50	-	0.8 M KPF_6 EC/DEC +1 wt% FEC	73
		$K_{1.81}Fe_{0.90}Mn_{0.10}[Fe(CN)_6]_{0.95}·0.92H_2O$	2.0-4.5		76/800	40/300	-	0.8 M KPF_6 EC/DEC +5 wt% FEC	74
		$K_{1.47}Fe_{0.5}Mn_{0.5}[Fe(CN)_6]·1.26H_2O$	2.0-4.5	155.3	55.9/200	68.5/450	-	1 M KPF_6 EC/DEC/PC	75
		$K_{1.23}Fe_{0.42}Mn_{0.45}Sn_{0.13}[Fe(CN)_6]_{0.94}·1.35H_2O$	2.0-4.5	97.4	47.1/200	61/300	-	1 M KPF_6 EC/DEC/PC	76
Indirect regulation	Morphology design	$KFe[Fe(CN)_6]_{0.82}·2.87H_2O$	2.0-4.5	118.7	71.9/200	80.49/1000	-	1 M KPF_6 EC/DEC/PC	77
		$K_{1.69}Fe[Fe(CN)_6]_{0.90}·0.4H_2O$	2.0-4.5	140	120/100	85/100	-	0.5 M KPF_6 EC/DEC + FEC	78
		$K_{1.4}Fe_4[Fe(CN)_6]_3$	2.0-4.0	71	24.9/600	75.2/100	-	0.5 M KPF_6 EC/DEC + 5 wt% FEC	79
		$K_{0.0216}FeFe(CN)_6·3.03H_2O$	2.0-4.5	127.2	86.7/3000	85.8/2000	-	1 M KPF_6 EC/PC +5 wt% FEC	80

View Article Online
DOI: 10.1039/D6SC02904C

		$K_{0.220}Fe[Fe(CN)_6]_{0.805}\cdot\square_{0.195}\cdot 4.01H_2O$	2.0-4.0	76.7	36.0/400	~86.5/150	44	0.8 M KPF_6 EC/DEC	80
	Hybridization with conductive materials	$K_{1.87}Fe[Fe(CN)_6]_{0.97}\cdot\square_{0.03}\cdot 0.84H_2O$	2.0-4.2	88.5	72.1/1000	86.8/500	72.67	0.8 M KPF_6 EC/DEC	81
		$K_{0.97}Fe[Fe(CN)_6]_{0.83}\cdot\square_{0.17}\cdot 0.28H_2O$	1.5-4.0	108.6	35.5/500	-	62.8	0.8 M KPF_6 EC/DEC + 2 wt% FEC	82
		$K_{1.59}Fe[Fe(CN)_6]_{0.90}\cdot 0.30H_2O$	2.5-4.3	121.8	-	96.5/800	-	0.5 M KPF_6 EC/DEC	84
		-	2.0-4.5	≈143.8	81.3/1000	87.4/500	-	3 M KPF_6 DEGDME	85
	Electrolyte modification	$K_2Fe[Fe(CN)_6]$	2.5-4.3	~106	-	90/50	~85	PEO-KTFSI	86
		$K_{1.92}Fe[Fe(CN)_6]_{0.94}\cdot 0.5H_2O$	2.0-4.4		76.2/200	81.3/600	86.6	1 M KFSI MeTMS/TTE	91

Annotation: Diethylene glycol dimethyl ether (DEGDME), ethylene carbonate/diethyl carbonate (EC/DEC), fluoroethylene carbonate (FEC), triethyl phosphate (TEP), propylene carbonate (PC), polyethylene oxide (PEO), 3-methylsulfolane (MeTMS), 1,1,2,2-tetrafluoroethyl-2,2,3,3-tetrafluoropropylether (TTE).

To further advance the electrochemical performance of these materials, we suggest the following aspects should be taken into consideration: First, precise regulation of defects and crystalline water content is essential. For example, optimizing synthesis conditions through coprecipitation (such as slow dropwise addition, low-temperature reaction), which are expected to reduce $[Fe(CN)_6]^{4-}$ vacancy defects. In addition, the introduction of coordination protectants (e.g., citric acid or EDTA-2K) can be utilized to preferentially coordinate with Fe^{2+}, thereby suppressing hydrolysis side reactions and lowering crystalline water content. Second, constructing a composite conductive network is an effective strategy to enhance charge transport. Compositing iron-based Prussian blue analogues with carbon materials or modifying their surface with conductive polymers can significantly reduce interfacial impedance, improve surface charge transfer kinetics, and thereby enhance rate capability. Meanwhile, a thin and uniform coating strategy using conductive materials should be developed to minimize the amount of non-electrochemically active conductive additives. Third, electrolyte formulation and interface stability require systematic optimization. Exploring novel electrolyte systems or incorporating sulfur-containing additives can be helpful to stabilize the electrode-electrolyte interface, mitigate side reactions and enhance overall battery performance. Forth, rational doping with metal elements (e.g., transition metal element Mn, Co, Ni) can disorder atomic arrangement, generate anisotropic stress fields which effectively dissipate mechanical stresses, thereby improving the structural integrity of the electrode as well as the electrochemical performances. Finally, a deeper understanding of material behavior and potassium storage mechanisms should be pursued through advanced characterization techniques such as in situ XRD and EXAFS, combined with theoretical modeling (e.g., DFT calculations) to probe structural and electronic influences on performance. On this basis, using artificial intelligence for material screening and optimization (such as predicting defect formation energies, ion diffusion energy barriers) is also expected to accelerate the research and development of next-generation FeHCF cathodes.

Conflicts of interest
There are no conflicts to declare.

Acknowledgements
This work was supported by the National Natural Science Foundation of China (52202286, 22309002), the open research fund of Guangxi Key Laboratory of Advanced Structural Materials and Carbon Neutralization (GXAMCN25-1), Natural Science Foundation of Zhejiang Provincial (LY24B030006), Science and Technology Plan Project of Wenzhou Municipality (ZG2024055), China National Postdoctoral Program for Innovative Talents (BX20250118), and Anhui Postdoctoral Scientific Research Program Foundation (2025B1045), the Fundamental Research Funds of Zhejiang Sci-Tech University (26202157-Y), Qingchuang Technology Support Program of the University in Shandong Province (2024KJH080), Shandong Provincial Natural Science Foundation (ZR2024MB153), Yantai Science and Technology Innovation Development Program (Basic Research Category, 2024JCYJ042).

References

1. B. Dunn, H. Kamath and J. M. Tarascon, *Science*. 2011, **334**, 928-935.
2. M. Sha, L. Liu, H. Zhao and Y. Lei. *Energy Environ. Mater*., 2020, **3**, 56-66.
3. Z. Yang, J. Zhang, M. C. Kintner-Meyer, X. Lu, D. Choi, J. P. Lemmon and J Liu. *Chem. Rev*., 2011, **111**, 3577-3613.
4. T. M. Gür. *Energy Environ. Sci*., 2018, **11**, 2696-2767.
5. J. Wang, Y. Zhou, Y. Zhuo, K. Fang, S. Wang, B. Zhao, J. Zhou and H. Wang. *Chem. Sci*., 2025, **16**, 552-574.
6. C. Peng, S. Liang, Y. Yu, L. Cao, C. Yang, X. Liu, K. Guo, P. Müller-Buschbaum, Y. Cheng and C. Wang. *Carbon Neutralization*. 2024, **3**, 1036-1091.
7. Y. Gao, H. Zhang, J. Peng, L. Li, Y. Xiao, L. Li, Y. Liu, Y. Qiao and S. L. Chou. *Carbon Energy*. 2024, **6**, e464.
8. F Wang, Z Jiang, Y Zhang, Y Zhang, J Li, H Wang, Y. Jiang, G. Xing, H. Liu and Y Tang. *eScience*. 2024, **4**, 100181.
9. H. Zhang, Y. Gao, J. Peng, Y. Fan, L. Zhao, L. Li, Y. Xiao, W. Pang, J. Wang and S. L. Chou, *Angew. Chem. Int. Ed*. 2023, **62**, 202303953.
10. J. Chen, X. Wu, Z. Luo, X. Ren, J. Chen, M. Chen, C. Xu, Y. Xiao and W. Yang. *Chem. Sci*. 2026.
11. S. Wang, X. Fu and S. Yao. *Acta Phys.-Chim.Sin*., 2026, **42**, 100206.
12. X. Zhou, B. Wen, Y. Cai, X. Chen, L. Li, Q. Zhao, S. L. Chou and F. Li, *Angew. Chem. Int. Ed*., 2024, **63**, 202402342.
13. N. Zhang, X. Chen, M. Yu, Z. Niu, F. Cheng and J. Chen, *Chem. Soc. Rev*., 2020, **49**, 4203.
14. L. Zhang, J. Xiao, X. Xiao, W. Xin, Y. Geng, Z. Yan and Z. Zhu. *eScience,* 2024, **4**, 100205.
15. J. H. Nguyen, A. Rana, K. Shiprath, B. R. Bhagat, S. Paul, S. Chatterjee, N. Roy, I. Das, B. Das, A. Banerjee and J. E. Dick. *Chem. Sci*., 2026, **17**, 2302-2316.
16. R. Xu, X. Gao,Y. Chen, X. Chen and L. Cui. *Chin. Chem. Lett*., 2024, **35**, 109852.
17. B. He, Y. Ling, Z. Wang, W. Gong, Z. Wang, Y. Liu, T. Zhou, T. Xiong, S. Wang, Y. Wang, Q. Li, Q. Zhang and L. Wei. *eScience,* 2024, **4**, 100293.
18. W. Kou, Z. Fang, H. Ding, W. Luo, C. Liu, L. Peng, X. Guo, W. Ding and W. Hou. *Adv. Funct. Mater*., 2024, **34**, 2406423.
19. L. Zhao, X. Gao, Q. Gu, X. Ge, Z. Ding, Z. Liu and W. Luo. *eScience,* 2024, **4**, 100201.
20. X. Li, X. Su, T. Su, L. Chen and Z. Su. *Chem. Sci*. 2025, **16**, 5353-5368.
21. J. Cao, K. Zhang, J. Yang, Z. Gu and X. Wu. *Chin. Chem. Lett*., 2024, **35**, 109304.
22. Y. Zhang, S. Li, Q. Yang, T. Huang, S. Shi, Z. Chen, T. Huo, X. Bai, M. Li, G. Yu, W. Zhang, X. Zhou, L. Li, K. Lei and S. Zheng. *Adv. Funct. Mater*., 2026, **36**, e10812.
23. S. Zhao, B. Zhang, L. Li, P. Zhang, G. Li, Z. Zhu, Y. Choi, L. Dong, M. Luo and S. Guo. *J. Am. Chem. Soc*., 2025, **147**, 669-677.
24. S. Komaba, T. Hasegawa, M. Dahbi and K. Kubota. *Electrochem. Commun*., 2015, **60**, 172-175.
25. L. Song, S. Zhang, L. Duan, R. Li, Y. Xu, J. Liao, L. Sun, X. Zhou and Z. Guo. *Angew. Chem. Int. Ed*., 2024, **63**, e202405648.
26. M. Ye, Y. Guan, R. Xu, P. Wang, Y. Zhang, J. Yu, D. Li, L. Li, Q. Zhao, Z. Wang, J. Liang and Y. Wu. *J. Energy Chem*., 2025, **106**, 650-670.
27. C. A. Nason and Y. Xu. *eScience,* 2024, **4**, 100183.
28. W. Xia, F. Ji, Y. Liu, Z. Han, K. Li, J. Lu, W. Zhai, D. Li and L. Ci. *Sci. Bull*., 2024, **69**, 3371-3383.
29. X. Zhang, T. Xiong, B. He, S. Feng, X. Wang, L. Wei and L. Mai. *Energy Environ. Sci*., 2022, **15**, 3750-3774.
30. C. Vaalma, D. Buchholz and S. Passerini. *Curr. Opin. Electrochem*., 2018, **9**, 41-48.
31. Q. Yao and C. Zhu. *Adv. Funct. Mater*., 2020, **30**, 2005209.
32. Y. Choi, B. Zhang, S. Zhao, J. Feng, X. Han, Z. Zhu, X. Zhao, K. Liu and S. Guo. *J. Am. Chem. Soc*., 2026, **148**, 16668-16678.
33. Y. Chen, W. Luo, M. Carter, L. Zhou, J. Dai, K. Fu, S. Lacey, T. Li, J. Wan, X. Han, Y. Bao and L. Hu. *Nano Energy,* 2015, **18**, 205-211.
34. J. Zheng, C. Hu, L. Nie, H. Chen, S. Zang, M. Ma and Q. Lai. *Adv. Mater. Technol*., 2023, **8**, 2201591.
35. A. Eftekhari, Z. Jian and X. Ji. *ACS Appl. Mater. Interfaces*., 2017, **9**, 4404-4419.
36. S. Qiao, Q. Zhou, H. Liu, S. Dou and S. Chong. *Nano Lett*., 2024, **24**, 15167-15177.
37. X. Li, T. Guo, Y. Shang, T. Zheng, B. Jia, X. Niu, Y. Zhu and Z. Wang. *Adv Mater*., 2024, **36**, 2310428.
38. J. Chen, A. M. Rao, C. Gao, J. Zhou, L. Cha, X. Yuan and B. Lu. *Nano Res*., 2024, **17**, 9671-9678.
39. J. Hao, K. Xiong, J. Zhou, A. M. Rao, X. Wang, H. Liu and B. Lu. *Energy Environ. Mater*., 2022, **5**, 261-269.
40. Z. Xiao, F. Xia, L. Xu, X. Wang, J. Meng, H. Wang, X. Zhang, L. Geng, J. Wu and L. Mai. *Adv. Funct. Mater*., 2022, **32**, 2108244.
41. X. Lin, J. Huang, H. Tan, J. Huang and B. Zhang. *Energy Storage Mater*., 2019, **16**, 97-101.
42. J. Liao, C. Chen, Q. Hu, Y. Du, Y. He, Y. Xu, Z. Zhang and X. Zhou. *Angew. Chem. Int. Ed*., 2021, **133**, 25779-25786.
43. S. S. Fedotov, N. D. Luchinin, D. A. Aksyonov, A. V. Morozov, S. V. Ryazantsev, M. Gaboardi, J. R. Plaisier, K. J. Stevenson, A. M. Abakumov and E. V. Antipov. *Nat*. *Commun*., 2020, **11**, 1484.
44. J. Ge, L. Fan, A. M. Rao, J. Zhou and B. Lu. *Nat*. *Sustain*., 2022, **5**, 225-234.
45. L. Deng, J. Qu, X. Niu, J. Liu, J. Zhang, Y. Hong, M. Feng, J. Wang, M. Hu, L. Zeng, Q. Zhang, L. Guo and Y. Zhu. *Nat*. *Commun*., 2021, **12**, 2167.
46. Y. Xia, W. Jin, Yanyuan Qi, Hang Li, Zelang Jian and Wen Chen. *Chinese Chemical Letters.,* 2021, **32**, 2433-2437.
47. C.-W. Chou and H.-Y. Tuan. *Adv. Funct. Mater*., 2025, **35**, 2418680.
48. M. Tang, Y. Wu, Y. Chen, C. Jiang, S. Zhu, S. Zhuo and C. Wang. *J. Mater. Chem. A*., 2019, **7**, 486-492.
49. Y. Hu, Y. Gao, L. Fan, Y. Zhang, B. Wang, Z. Qin, J. Zhou and B. Lu. *Adv. Energy Mater*., 2020, **10**, 2002780.
50. Q. Zhao, J. Wang, Y. Lu, Y. Li and G. Liang, J. Chen. *Angew. Chem. Int. Ed*., 2016, **55**, 12528-12532.
51. B. Zhou, Y. Gao, X. Lin, X. Lin, B. Yang, N. Kang, Y. Qiao, H. Zhang, L. Li and S. L. Chou. *Chem. Sci.*, 2025, **16**, 13594-13628.
52. X. Wang, C. Gao, S. Zhang, J. Wang, Y. Lou, F. Kang and D. Zhai.

Adv. Energy Mater., 2024, **14**, 2401708.
53. Y. Xu, S. Duan, Y. Sun, D. Bin, X. Tao, D. Zhang, Y. Liu, A. Cao and L. Wan. *J. Mater. Chem. A*., 2019, **7**, 4334-4352.
54. J. Wang, C. Xing, Q. Yang and X. Zhou. *Chin Sci Bull*., 2026, **71**, 2064-2080.
55. G. Du, M. Tao, J. Li, T. Yang, W. Gao, J. Deng, Y. Qi, S.-J. Bao and M. Xu. *Adv. Energy Mater*., 2020, **10**, 1903351.
56. R. Rajagopalan, Y. Tang, X. Ji, C. Jia and H. Wang. *Adv. Funct. Mater*., 2020, **30**, 1909486.
57. Y. Liu, C. Gao, L. Dai, Q. Deng, L. Wang, J. Luo, S. Liu and N. Hu. *Small,* 2020, **16**, 2004096.
58. L. Xue, Y. Li, H. Gao, W. Zhou, X. Lü, W. Kaveevivitchai, A. Manthiram and J. B. Goodenough. *J. Am. Chem. Soc*., 2017, **139**, 2164-2167.
59. S. H. Jung, P. T. Huong, M. Mapari, T. T. Tung and T. Y. Kim. *Batteries & Supercaps.,* 2024, **7**, e202400091.
60. B. Huang, Y. Shao, Y. Liu, Z. Lu, X. Lu and S. Liao. *ACS Appl. Energy Mater*., 2019, **2**, 6528-6535.
61. L. Li, Z. Hu, Y. Lu, C. Wang, Q. Zhang, S. Zhao, J. Peng, K. Zhang, S. L. Chou and J. Chen. *Angew. Chem. Int. Ed*., 2021, **133**, 13160-13166.
62. W. Yan, X. Feng, X. Min, B. Ma, Y. Liu, R. Mi, X. Wu, W. Wang, Z. Huang and M. Fang. *J. Electrochem. Soc*., 2024, **171**, 080529.
63. A. Li, Y. Man, J. Liao, L. Duan, X. Ji and X. Zhou. *Nano Lett*., 2023, **23**, 10066-10073.
64. Y. Wei, S. Zhang, D. Zhai and F. Kang. *Battery Energy,* 2023, **2**, 20220027.
65. X. Ma, Y. Guo, C. Yu, X. Chen, L. Gui, N. Cheng, J. Sun, P. Chen, J. Chen, Z. Zi and J. Dai. *J. Alloys Compd*., 2022, **904**, 164049.
66. Z. Wang, W. Zhuo, J. Li, L. Ma, S. Tan, G. Zhang, H. Yin, W. Qin, H. Wang, L. Pan, A. Qin and W. Mai. *Nano Energy,* 2022, **98**, 107243.
67. R. Ma, Z. Wang, Q. Fu, W. Zhou, Y. Mo, J. Tu, Z. Wang, P. Gao, C. Fan and J. Liu. *J. Energy Chem*., 2023, **83**, 16-23.
68. W. Shu, M. Huang, L. Geng, F. Qiao and X. Wang. *Small,* 2023, **19**, 2207080.
69. S. Zhang, C. Gao, X. Wang, W. Li, C. Yang, F. Kang and D. Zhai. *Nano Lett*., 2025, **25**, 14166−14174.
70. L. Duan, Y. Du, Y. Liu, H. Tang, C. Zhou, D. Kim, Z. Lin and X. Zhou. *Chem. Soc. Rev.,* 2025, **54**, 11740-11826.
71. L. Song, M. Tan, S. Zhang, H. Tang, H. Qi, Z. Yuan, L. Sun, X. Zhou and Z. Guo. *Angew. Chem. Int. Ed*., 2026, **65**, e6795880.
72. J. Kim, J. Lee, J. Baek, W. Jeong, S. Seo, S. Lee, S. Lee, B. Sambandam, V. Mathew and J. Kim. *Energy & Fuels*., 2024, **38**, 22574-22583.
73. B. Huang, Y. Liu, Z. Lu, M. Shen, J. Zhou, J. Ren, X. Li and S. Liao. *ACS Sustain. Chem. Eng*., 2019, **7**, 16659-16667.
74. R. Sun, X. Feng, J. Chen, Y. Zhang, R. Wang, Y. Chen, B. Han, K. Xia, Q. Gao and C. Zhou. *J. Power Sources*., 2023, **556**, 232406.
75. Q. Zhou, H. Liu, S. Dou and S. Chong. *ACS nano*., 2024, **18**, 7287-7297.
76. H. Huang, S. Qiao, B. Lv, H. Liu, S. Dou and S. Chong. *Nano Lett*., 2025, **25**, 15062−15071.
77. S. Chong, Y. Chen, Y. Zheng, Q. Tan, C. Shu, Y. Liu and Z. Guo. J. Mater. Chem. A., 2017, **5**, 22465-22471.
78. G. He and L. F. Nazar. *ACS Energy Lett*., 2017, 2, 1122-1127.
79. M. Qin, W. Ren, J. Meng, X. Wang, X. Yao, Y. Ke, Q. Li and L. Mai. *ACS Sustain. Chem. Eng*., 2019, **7**, 11564-11570.
80. Y. Xu, Y. Du, L. Song, S. Zhang, Z. Yuan, J. Wang, H. Liu, L. Sun, X. Zhou and Z. Guo. *Angew. Chem. Int. Ed*., 2025, **64**, e202422723.
81. Q. Xue, L. Li, Y. Huang, R. Huang, F. Wu and R. Chen. *ACS Appl. Mater. Interfaces*., 2019, **11**, 22339-22345.
82. M. Zhou, X. Tian, Y. Sun, X. He, H. Li, T. Ma, Q. Zhao and J. Qiu. *Nano Res.,* 2023, **16**, 6326-6333.
83. Y. Zhu, Y. Yin, X. Yang, T. Sun, S. Wang, Y. Jiang, J. Yan and X. Zhang. *Angew. Chem. Int. Ed*., 2017, **56**, 7881-7885.
84. Y. Wei, H. Wang, J. Wang, C. Gao, H. Zhang, F. Yuan, J. Dong, D. Zhai and F. Kang. *ACS Appl. Mater. Interfaces*., 2021, **13**, 54079-54087.
85. B. Liu, Z. Li, Y. Xu, M. Qiu, J. Li, S. Gao, R. Yao, X. Song and Y. Li. *Adv. Funct. Mater*., 2025, **35**, e09849.
86. A. D. Khudyshkina, P. A. Morozova, A. J. Butzelaar, M. Hoffmann, M. Wilhelm, P. Theato, S. S. Fedotov and F. Jeschull. *ACS Appl. Polym. Mater*., 2022, **4**, 2734-2746.
87. Y. Lin, J. Liu, L. Shi, N. Guo, Z. Sun, C. Geng, J. Jiang, Q. Zhuang, Y. Chen and Z. Ju. *J. Colloid Interface Sci*., 2022, **623**, 1-8.
88. Z. Wang, K. Luo, Y. Mo, J. Ke, W. Zhou, S. Chen, P. Gao and J. Liu. *Adv. Funct. Mater*., 2024, **35**, 2417243.
89. X. Wu, Z. Jian, Z. Li and X. Ji. *Electrochem. Commun*., 2017, **77**, 54-57.
90. C. Zhang, Y. Xu, M. Zhou, L. Liang, H. Dong, M. Wu, Y. Yang and Y. Lei. *Adv. Funct. Mater.,* 2017, **27**, 1604307.
91. Z. Yuan, L. Chen, J. Liao, L. Song, A. Chen, D. Yan, J. Wang and X. Zhou. *Angew. Chem. Int. Ed*., 2026, **65**, e23473.

View Article Online
DOI: 10.1039/D6SC02904C

No primary research results, software or code have been included and no new data were generated or analysed as part of this review.